Interface effects of Pb films on $TlBiSe_2$ and Bi_2Se_3 topological insulators

Roberto Flammini [1,*] Oreste De Luca [2,3,4,*] Martina Casciaro [2,3] Tommaso Caruso [2,3] Fabio Biffoli,[5] Daniela Pacilé,[2,3] Khatira Z. Mehtiyeva [6] Ziya S. Aliev [6,7] Alexey Barinov,[8] Alfonso Policicchio [3] Anastasia G. Ryabishchenkova [9] Fabio Ronci [1] Stefano Colonna [1] Evgueni V. Chulkov [10,11,12,13] Raffaele G. Agostino [2,3] Sergey V. Eremeev [14] and Marco Papagno [2,3,†]

[1]*Istituto di Struttura della Materia-CNR (ISM-CNR), Via del Fosso del Cavaliere, 00133 Roma, Italy*

[2]*Laboratorio di Spettroscopia Avanzata dei Materiali, STAR IR, Via Tito Flavio, Università della Calabria, 87036 Rende (CS), Italy*

[3]*Dipartimento di Fisica, Università della Calabria, Via P. Bucci, I-87036 Rende (CS), Italy*

[4]*CNR-Nanotec, UoS di Cosenza, Dipartimento di Fisica, Università della Calabria, 87036 Arcavacata di Rende (CS), Italy*

[5]*Department of Chemistry Ugo Schiff, University of Florence, Via della Lastruccia 3, 50019 Sesto Fiorentino, Firenze, Italy*

[6]*Baku State University, Baku AZ1148, Azerbaijan*

[7]*National Aviation Academy of Azerbaijan, Baku AZ1045, Azerbaijan*

[8]*Sincrotrone Trieste S.C.p.A., Area Science Park, I-34012 Basovizza, Trieste, Italy*

[9]*Rzhanov Institute of Semiconductor Physics, Siberian Branch, Russian Academy of Sciences, Novosibirsk 630090, Russia*

[10]*Departamento de Polímeros y Materiales Avanzados: Física, Química y Tecnología, Facultad de Ciencias Químicas, Universidad del País Vasco UPV/EHU, 20080 San Sebastián/Donostia, Spain*

[11]*Donostia International Physics Center (DIPC), 20018 Donostia-San Sebastián, Basque Country, Spain*

[12]*Centro de Física de Materiales (CFM-MPC), Centro Mixto CSIC-UPV/EHU, 20018 Donostia-San Sebastián, Basque Country, Spain*

[13]*Laboratory of Electronic and Spin Structure of Nanosystems, Saint Petersburg State University, 198504 Saint Petersburg, Russia*

[14]*Institute of Strength Physics and Materials Science, Siberian Branch, Russian Academy of Sciences, 634055 Tomsk, Russia*

(Received 6 March 2026; revised 12 May 2026; accepted 20 May 2026; published 1 July 2026)

We present an experimental investigation of the Pb-induced changes on the electronic structure of selected topological insulators, namely, $TlBiSe_2$ and Bi_2Se_3. Using spatially resolved and surface-sensitive techniques, including micro-angle-resolved photoemission (μ-ARPES) and micro-core-level photoemission (μ-PES), we track the evolution of the electronic states during adsorbate growth. For low Pb coverage on $TlBiSe_2$, we identify the formation of a disordered interface. For thicker films, μ-ARPES measurements clearly resolve well-defined electron confinement (quantum well) states within the metallic Pb layers and no migration of the topological surface state onto the Pb film is observed. Furthermore, μ-PES results on both Pb/$TlBiSe_2$ and Pb/Bi_2Se_3 heterostructures can be rationalized in terms of a significant chemical interaction between Pb and Se, leading to substantial surface degradation and Bi atom segregation. The *ab initio* modeling performed on the adsorption of lead on topological insulator surfaces, which includes the consideration of the swapping of Pb adsorbates with Bi substrate atoms, validates the scenario derived from experimental observations. It also suggests that the development of a disordered interface is due to the formation of PbSe nuclei, whose size is constrained by the compressive stresses exerted by the TI substrate.

DOI: 10.1103/nxxg-r5b2

I. INTRODUCTION

In recent decades, the study of structural and electronic phenomena at interfaces between dissimilar materials has emerged as a fertile ground for discovering intriguing physics and developing advanced nanotechnology applications. By carefully engineering such interfaces, it is possible to generate entirely unique electronic properties that do not exist in the constituent bulk materials [1–6] or to transfer exotic electronic behavior from one material to the other via the proximity effect [6–11].

A particularly exciting frontier in this field involves creating topological superconductors (TSCs), typically by bringing a conventional superconductor into contact with a topological insulator (TI) [12–14]. TIs are a unique class of quantum materials characterized by an insulating bulk while possessing metallic, spin-polarized topological surface states (TSSs) that are protected by time-reversal symmetry [15–18]. When interfaced with a superconductor, the TSS may relocate to the superconducting overlayer through the proximity effect, thereby acquiring superconducting properties and potentially hosting non-Abelian quasiparticles known as Majorana modes [19,20]. The realization of these modes is not only a major

*These authors contributed equally to this work.
†Contact author: marco.papagno@unical.it

goal in fundamental condensed matter physics but also holds promise for quantum computing and applications in spintronics and quantum memory elements [13,21,22].

The interface between an *s*-wave superconductor (Pb) with a representative TI, Bi_2Se_3[23], as well as the previously investigated Pb/$TlBiSe_2$ system [24], can offer an ideal platform for exploring new phenomena. Lead is characterized by a relatively high critical temperature ($T_C = 7.2$ K) [25–28], thus providing a strong superconducting environment. Indeed, the successful realization of a TSC has recently been suggested based on angle-resolved photoemission spectroscopy (ARPES) studies of heterostructures composed of epitaxial Pb films grown on $TlBiSe_2$ [24]. A remarkable observation in that study was the apparent migration of the substrate-associated TSS to the surface of superconducting Pb films with thicknesses of up to approximately 6.6 nm (more than 20 monolayer). Similar proximity effects have been theoretically proposed and experimentally investigated in other related systems, for example, the emergence of spin-polarized topological quantum well (QW) states in Pb films grown on the topological semimetal Sb, as revealed by ARPES measurements and spin-resolved density functional theory calculations [29].

These findings have generated significant interest in the potential emergence of topological physics in heterostructure systems. However, the exact interfacial mechanisms driving the migration or disappearance of topological properties remain poorly understood, and some recent experimental results regarding the transfer of the TSS have been questioned [30]. Several studies concerning Pb/TI heterostructures focused primarily on the electronic structure of the valence band at high Pb coverages (several monolayers), leaving the interface formation and electronic state evolution at varying stages of growth largely unexplored. The initial growth stages, where the first few layers are deposited, are often critical in determining the final electronic and chemical structure of the entire heterostructure.

In this work, we address these gaps by providing a surface-sensitive and spatially resolved photoemission investigation of Pb films grown on two distinct topological systems: $TlBiSe_2$ and Bi_2Se_3. Performing μ-ARPES and μ-photoemission spectroscopy (μ-PES) measurements on the same sample spots, we unveil the electronic states of Pb/$TlBiSe_2$ and Pb/Bi_2Se_3 systems for different Pb coverages. Our experimental findings, supported by *ab initio* simulations of Pb adsorption on topological insulator surfaces, evidence significant surface degradation caused by the development of a disordered PbSe clusters at the interface and Bi atoms segregation.

II. METHODS

Single crystals of Bi_2Se_3 and $TlBiSe_2$ were synthesized using high-purity elements via the Bridgman method. The crystalline quality was verified by x-ray diffraction measurements. All of the investigated samples were sourced from the same ingot. The samples were glued to sample holders and cleaved under ultrahigh vacuum (UHV) conditions. The cleaved surfaces remained stable for several days, provided they were kept under UHV. Lead was deposited using a temperature-controlled Knudsen cell in UHV conditions onto the TI samples kept at liquid nitrogen (LN) temperature with a deposition rate of 0.33 Å/min. The Pb coverage will be hereafter reported in terms of monolayer (ML), where 1 ML corresponds to 0.286 nm, i.e., the interplanar spacing along the (111) direction. Immediately after deposition, the sample was transferred to the UHV-connected photoemission chamber, where it was maintained at LN temperature throughout all measurements.

Scanning photoemission microscopy (SPEM), spatially resolved μ-PES and μ-ARPES measurements were carried out at the Spectromicroscopy beamline [31] at the Elettra synchrotron radiation source at LN temperature under UHV conditions. Photons were focused through a Schwarzschild objective to achieve a sub-μm beam size spot. The total energy resolution was set to 70 meV with an angle resolution of 0.6°. μ-ARPES maps were acquired at photon energies of 74 and 27 eV along the $\overline{\mathrm{M\Gamma M}}$ direction of the projected surface Brillouin zone, with an acceptance angle of $\pm 7.5° \pm 0.3°$. Since μ-photoemission measurements performed at 74 eV provide enhanced surface sensitivity and improved resolution of the topological surface states (see Fig. 7), we present the photoemission data acquired at this photon energy. SPEM intensity images were acquired with 74 eV photon energy, integrating the photoemission spectra across an energy range of ∼3.5 eV. μ-PES spectra were acquired at 74 eV on the same sample spot investigated by the μ-ARPES measurements. Core-level binding energies were calibrated relative to the Fermi level (E_F) with ± 0.02 eV indeterminacy. The Bi 5*d*, Se 3*d*, Tl 5*d*, and Pb 5*d* peaks were fitted with a linear combination of Lorentzian and Gaussian line shapes, with a Shirley background applied to all core-level spectra. For all core-level spectra, the asymmetry parameter was set to zero.

Electronic structure calculations were carried out within density functional theory using the projector augmented-wave method [32] as implemented in the VASP code [33,34]. The Hamiltonian contained scalar relativistic corrections and the spin-orbit coupling was taken into account when the structures were relaxed. Relaxation was performed using a conjugate-gradient algorithm. The generalized gradient approximation (GGA-PBE [35]) for the exchange-correlation energy and the DFT-D3 van der Waals (vdW) functional with Becke-Johnson damping [36] were applied for structure optimization.

The crystal structure of $TlBiSe_2$ is rhombohedral with 12 atomic layers and lattice parameters $a = 4.24$ Å and $c = 22.33$ Å [37]. The atomic coordinates were relaxed using a force tolerance criterion for convergence of 10^{-4} eV/Å and the convergence criterion for the total energy was 10^{-6} eV. The deposion of Pb on TI substrates ($TlBiSe_2$ and Bi_2Se_3) was modeled on 3×3 surface supercells. In case $TlBiSe_2$, a slab of four atomic layers Se-Bi-Se-Tl in which three upper Se-Bi-Se layers were allowed to relax while the bottom Tl layer was fixed and passivated by hydrogen. The charge on the passivated Tl (2.40*e*) is comparable to that in the $TlBiSe_2$ bulk (2.33*e*). This allows us to assume that the H-passivated Tl layer is in bulklike conditions, which makes it possible to use a thin slab to study processes on the surface. An additional layer of thallium on top, either full or partial, was also placed for individual structures on which lead deposition was considered. We considered single lead adatoms, their clusters, and a complete monolayer. In case modeling of Pb on Bi_2Se_3, the TI slab contains one 3×3 quintuple-layer block with the bottom

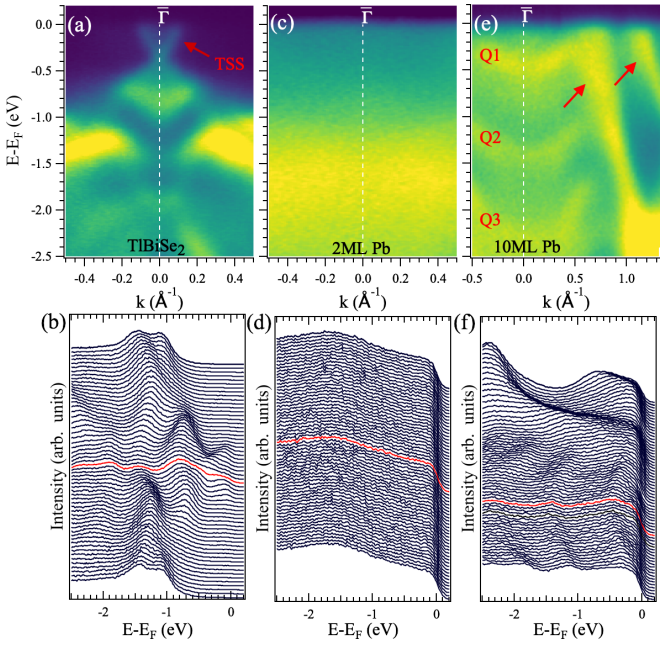

FIG. 1. μ-ARPES band structure and corresponding energy distribution curves acquired along $\overline{M}\overline{\Gamma}\overline{M}$ with 74 eV photon energy of (a), (b) pristine $TlBiSe_2$, and after deposition of (c), (d) 2 ML and (e), (f) 10 ML of Pb. TSS in (a) identifies the topological surface state, red curves in (b), (d), and (f) mark the energy distribution curves at $\overline{\Gamma}$, Q1, Q2, and Q3 in (e) the quantum well states of Pb.

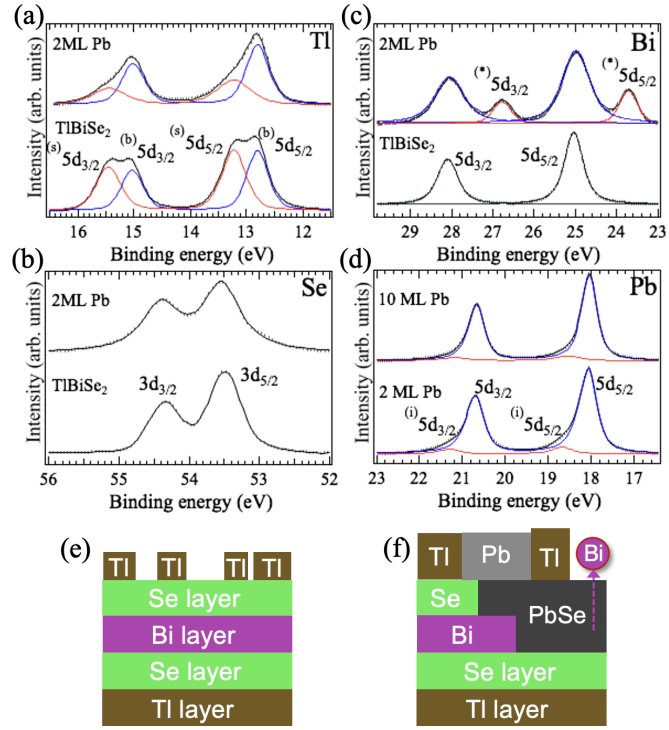

FIG. 2. μ-PES spectra for (a) Tl $5d$, (b) Se $3d$, and (c) Bi $5d$ states are shown for pristine $TlBiSe_2$ (bottom curve) and after 2 ML Pb deposition (top curve). (d) μ-PES spectra of the Pb $5d$ states after 2 ML (bottom curve) and 10 ML (top curve) Pb deposition on $TlBiSe_2$. For 10 ML Pb coverage, no photoelectrons from the substrate were detected. All core-level intensities have been rescaled to facilitate comparison. Sketch of (e) the cleaved $TlBiSe_2$ surface, (f) the formation of a disordered interface layer, Pb islands after deposition of 2 ML Pb and Bi atoms migration to the surface.

layer of Se fixed during relaxation. The $3 \times 3 \times 1$ k-point grid was used to sample the surface Brillouin zone.

For analysis of interactions between atoms on Pb/Tl surfaces, we use the projected crystal orbital Hamilton population (pCOHP) method [38,39] implemented within Local-orbital basis suite towards electronic structure reconstruction (LOBSTER) code [40].

III. RESULTS AND DISCUSSION

A. Pb/$TlBiSe_2$

Figures 1(a) and 1(b) display the μ-ARPES band structure and corresponding energy distribution curves measured on a freshly cleaved $TlBiSe_2$ sample along the $\overline{M}\overline{\Gamma}\overline{M}$ direction of the hexagonal (0001) (rhombohedral (111)) surface using 74 eV photons. A sharp and well-defined TSS is observed at the $\overline{\Gamma}$ point with the Dirac point energy situated at ~0.36 eV below the Fermi level (E_F) [41,42]. Additionally, several dispersive features are present at energies 0.7 eV below E_F, attributed to hybridized states of Tl/Bi $6p$ and Se $4p$ orbitals [37,43–45].

Upon depositing a 2 ML of Pb (see Fig. 8 for the SPEM image of the investigated Pb/$TlBiSe_2$ system) , both the characteristic band structure and the TSS of $TlBiSe_2$ disappear, as illustrated in Figs. 1(c) and 1(d), and nondispersive states emerge suggesting a disordered interface.

At higher coverages, Pb follows a layer-plus-island (Stranski-Krastanov) growth mode [46,47], enabling the formation of an ordered and thick film on top of the $TlBiSe_2$ surface. μ-ARPES results for both 10 ML [Figs. 1(e) and 1(f)] and 20 ML (not shown) Pb coverages show QW states due to the electron confinement within the Pb films [48–50]. These quantized states originate from Pb $6p$ orbitals and are characterized by upward parabolic dispersions with a band minimum at $\overline{\Gamma}$ (predominantly of $6p_z$ symmetry), alongside two bands (highlighted by two arrows) exhibiting downward dispersion and an unoccupied band maximum at $\overline{\Gamma}$ (with $6p_{x,y}$ symmetry). The highly ordered Pb film allows us to observe a peculiar behavior: the merging of the $6p_z$ and the inner $6p_{x,y}$ states at ~0.7 $Å^{-1}$ close to E_F [51–53].

It is observed that regardless of the Pb film thickness, the electronic states and the TSS of $TlBiSe_2$ are no longer detectable [Figs. 1(c)–1(f)]. Since the photon energy used in these measurements is extremely surface sensitive (with 74 eV photons only the topmost layers, approximately 8 Å, are probed), we conclude that, under these experimental conditions, no TSS is transferred to the Pb film.

Photoemission spectroscopy on core levels offers further insight into the Pb/$TlBiSe_2$ heterostructure. μ-PES on Pb/$TlBiSe_2$ are presented in Figs. 2(a)–2(d). Pristine $TlBiSe_2$ displays the Tl bulk $^{(b)}5d$ states, split into $5d_{3/2}$ and $5d_{5/2}$ by spin-orbit interaction at binding energies 15.03 and 12.78 eV, respectively [bottom curve in Fig. 2(a)] [54]. Additionally, components from surface Tl atoms ($^{(s)}5d$), shifted by 0.42 eV toward higher binding energy relative to the bulk components, are observed. This shift reflects the distinct electronic

environment of surface Tl atoms in $TlBiSe_2$, as demonstrated by detailed photoemission measurements performed at different photon energies [54]. 2 ML of Pb affects the relative intensity of the surface/bulk Tl 5*d* components [top curve in Fig. 2(a)]. However, no significant changes in the binding energies or additional photoemission structures are observed within the experimental resolution, suggesting a negligible Pb-Tl interaction.

Figure 2(b) (bottom curve) shows the Se $3d_{3/2}$ and $3d_{5/2}$ states at 54.33 and 53.48 eV for pristine $TlBiSe_2$ [24,54]. After deposition of 2 ML of Pb [Fig. 2(b), top curve] a relatively small energy shift (∼40 meV) of the Se 3*d* states toward higher binding energy is observed, accompanied by an increase of the full-width at half maximum from ∼0.50 eV to ∼0.70 eV.

The Bi 5*d* spectrum for pristine $TlBiSe_2$ in Fig. 2(c) (bottom curve) shows two peaks at 28.08 and 25.03 eV, corresponding to the $5d_{3/2}$ and $5d_{5/2}$ states, respectively. Two additional prominent features centered at 26.75 and 23.69 eV emerge upon deposition of 2 ML of Pb, which are reminiscent of the metallic 5*d* states [55] [labeled as $^{(*)}5d$ in the top curve of Fig. 2(c)]. Metallic Bi components have been previously observed in photoemission experiments after deposition of ultrathin films of Cr [56], Fe [56], Pb [30,57], and Au [56,58] on Bi_2Se_3, Ag on $Bi_{1.5}Sb_{0.5}Te_{1.7}Se_{1.3}$ [59], and Pb on magnetic TIs [54]. Although noble metal atoms may either substitute topmost layer atoms or intercalate into the van der Waals gaps, leaving the core levels of the surface atom relatively unchanged, Cr and Fe tend to interact with Se at the surface to form compounds such as Cr_xSe_y and Fe_xSe_y [53,60–62], significantly altering the Se 3*d* core-level spectrum.

The presented photoemission results suggest that a similar interaction may also occur in Pb/$TlBiSe_2$ [see Figs. 2(e) and 2(f)]: It has been experimentally established that the cleavage of $TlBiSe_2$ produces Tl islands on the surface [54,63], then in the initial stages of deposition Pb tends to fill the voids between the islands. As a consequence, the Tl islands tend to squeeze and coalesce, becoming taller and uncovering larger portions of the surface. Then, where the Pb atoms are directly in contact with the Se atoms, a compound of lead salt (PbSe) possibly forms, through the hybridization of Se 4*p* and Pb 6*p* states. The oxidation state of Se in lead salts is the same as that in $TlBiSe_2$ (−2), resulting in the same binding energy of the Se 3*d* states in the two compounds [64]. Interestingly, Pb–Se bonding induces unpaired electrons (dangling bonds) in the underlying Bi layer, making the segregation of Bi energetically favorable [65–67] and leading to an increase of the intensity of the $^{(*)}$Bi component [Fig. 2(c)]. We note that amorphous interfaces are also formed by depositing Pb ultrathin films on Bi_2Te_3 [68], Sb_2Te_3 [57] Bi_2Se_3 [30,57], magnetic TIs [46,47], and Si(111)-(6 × 6) [69]. We emphasize that a disordered interface inhibits the formation and propagation of Bloch-type waves and, in the case of topological insulators, causes the TSS to vanish or to be relocalized into the bulk [58,59,70,71].

The Pb 5*d* core-level results in Fig. 2(d) support this interpretation. Pb atoms experience different chemical environments already at 2 ML coverage. In addition to the sharp and intense 5*d* component at 20.69 and 18.06 eV (attributed to the bulk-related features of Pb [30,55]), broader and weaker

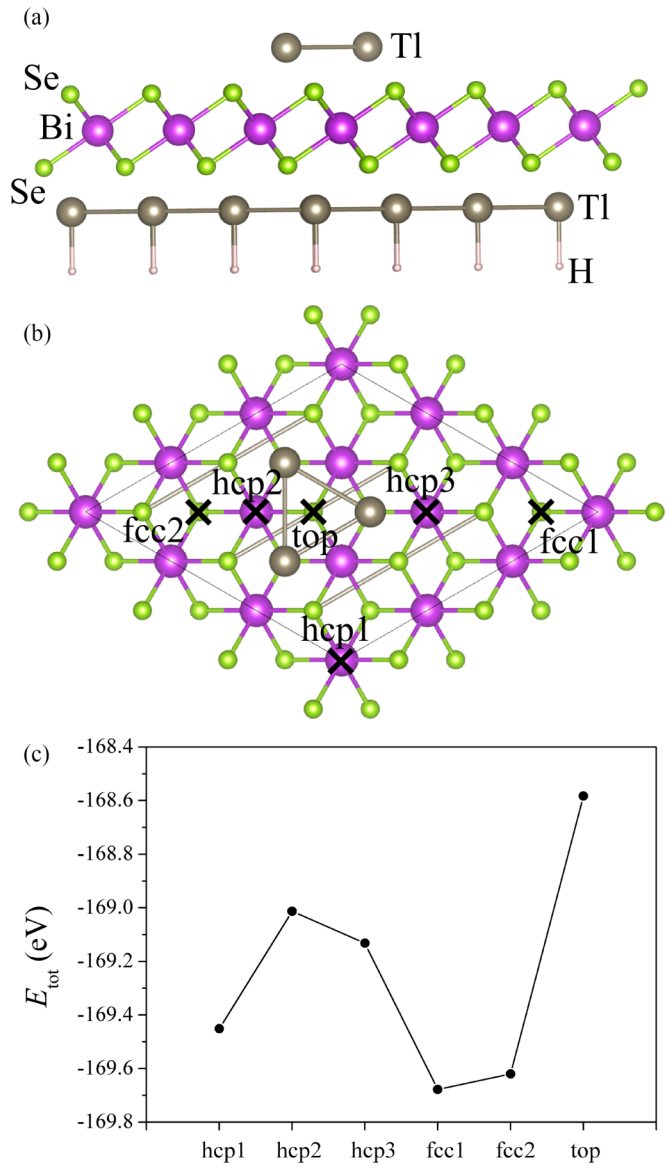

FIG. 3. Adsorption of single Pb adatom on $TlBiSe_2$ surface with mixed Tl/Se termination. Side and top views of the model are shown in (a) and (b), respectively. Crosses in (b) denote considered adsorption positions for Pb adatom and (c) shows calculated total energies in these positions. Solid line serves as a guide for the eyes.

features are observed (labeled $^{(i)}5d$ at 21.30 and 18.65 eV) and assigned to lead salt crystals, in agreement with the literature [72,73].

To complement our experimental findings and possibly reveal the preferred reaction mechanisms, we performed DFT calculations. Since cleaving $TlBiSe_2$ results in a surface composed of Tl islands atop a Se layer [54,63] (i.e., both Tl- and Se-terminated), we first considered the adsorption of a single Pb adatom on a surface containing a Tl island [see Figs. 3(a) and 3(b)]. Calculations show [Fig. 3(c)] that the most unfavorable adsorption position for Pb adatom is on the Tl island, while at the selenium termination, adsorption is preferable at the fcc positions compared to the hcp ones. However, in both cases, the farther the lead adatom is adsorbed from the

Tl island, the more energetically favorable it is. Thus, at the initial stage of deposition, the deposited Pb atoms will avoid the Tl islands and accumulate at the selenium termination.

To initiate the formation of the cubic PbSe phase, lead atoms are required to substitute bismuth atoms in the second layer. To understand how deposited lead affects interatomic bonds on the surface, we first evaluated the bond energies on the clean Se-terminated surface. The bond energies were estimated using integrated projected crystal orbital Hamilton population calculations (Fig. 9). We found that the strength of the bond between the bismuth atoms of the second layer ($Bi_{(2)}$) and the Se atoms of the third layer ($Se_{(3)}$) is approximately 1 eV lower than that between $Bi_{(2)}$ and the selenium of the topmost layer ($Se_{(1)}$). This is because $Se_{(3)}$ interacts strongly with the next layer Tl atom.

When a single Pb adatom resides on the surface [Fig. 10(a)], it strongly interacts with neighboring Se atoms [Fig. 10(b)]. These bonds are more than 1 eV stronger than bonds in the cubic PbSe bulk phase [Fig. 10(c)]. At the same time, the bonds between the Bi and Se atoms are no longer equivalent to the clean Se termination, but depend on the position of the Se-Bi pair relative to the Pb adatom [Fig. 10(b)]. In general, the $Se_{(1)}$-$Bi_{(2)}$ bonds are significantly weakened, while the $Bi_{(2)}$-$Se_{(3)}$ bonds are slightly strengthened compared to the clean Se termination.

After performing calculations for swapping the lead atom in the fcc position at the selenium termination and the nearest bismuth atom, we found that this process is unfavorable. The energy of such swapping is 0.715 eV [Fig. 4(a)]. As a result of this swapping, the energies of Pb-Se bonds are reduced compared to the initial Pb adatom position, while the bonds of the Bi atom, displaced to the adatom position, with neighboring $Se_{(1)}$ atoms become very strong, up to 3 eV. When no isolated Pb adsorbates are present and the smallest cluster (a trimer) is considered instead, substitution of Bi with Pb remains unfavorable, but its energy cost is reduced by about half to 0.374 eV [Fig. 11(a)]. Finally, when the amount of deposited lead becomes sufficient to form large clusters or islands (in the case of our simulation on a 3×3 supercell, this is a full Pb monolayer, see Fig. 4(b), swapping lead and bismuth becomes energetically favorable. The energy gain from swapping of one Pb-Bi pair is 0.363 eV [Fig. 4(c)] and increases sharply to 1.311 eV if three Pb-Bi pairs [Fig. 11(b)] are involved in the swapping. The result of such swapping can be considered as the formation of a seeding point for the cubic PbSe phase. Moreover, if the substituted bismuth atoms migrate away from the swapping sites [Fig. 4(d)], this reduces the energy by another 0.898 eV and the total energy gain with respect to the Pb monolayer becomes equal to 2.209 eV.

The observation that swapping becomes favorable upon formation of an extended Pb layer, whereas it is unfavorable for a single adsorbate or small clusters, arises from the modification of the bonding induced by the Pb overlayer. The formation of a Pb layer results in a huge softening of the $Se_{(1)}$-$Bi_{(2)}$ bond (down to 1.06 eV) and of the Pb-Se bond (down to 1.68 eV), compared to the adsorption of a single Pb adatom (2.60 eV); see Fig. 4(b). Such a significant decrease in bond energies should facilitate the processes of atomic rearrangement on the surface. As a result of swapping, the bonds between the displaced Bi atom and the nearest $Se_{(1)}$ atoms become an order of magnitude weaker [0.18 – 0.50 eV, Fig. 4(c)] compared to the case of Pb-Bi swapping on Se termination with a single adatom [Fig. 4(a)]. This weakening of the Bi-$Se_{(1)}$ bonds will promote the activation of the Bi migration away from the forming PbSe nucleus.

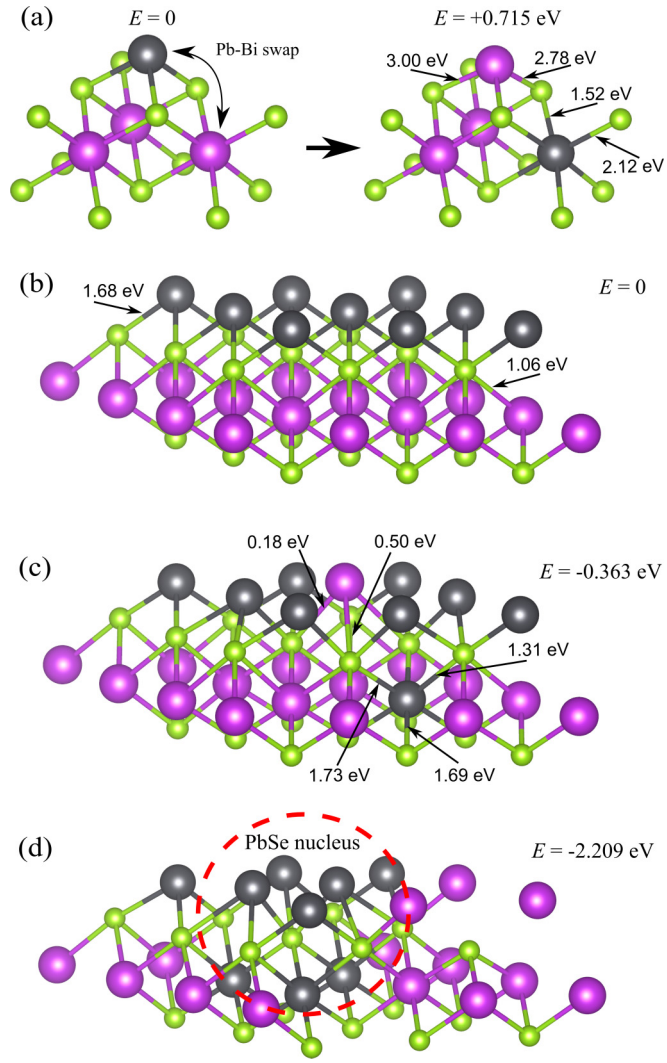

FIG. 4. (a) Swapping of single Pb adatom and nearest Bi atom (only the immediate surroundings of the swapping pair are shown for clarity). Left side: Initial positions of the Pb and Bi atoms; right side: Atomic configuration after swapping. Relative total energies are shown above the atomic models. The bond energies for Pb-Se and Bi-Se after swapping are marked. (b) Se terminated surface covered by Pb monolayer. Pb-$Se_{(1)}$ and $Se_{(1)}$-$Bi_{(2)}$ bond energies are indicated. (c) Pb-Bi swapping in case of Se termination with Pb coverage. Bond energies for selected atomic pairs are shown. (d) Formation of PbSe nucleus as a result of triple Pb-Bi swapping and migration of displaced Bi atoms away of the nucleus. In (c) and (d), the total energies relative to that in the structure with ideal Pb monolayer, taken as zero [(b)] are indicated.

However, a complete reversal of the lead and bismuth layers within the 3×3 supercell is unfavorable by 0.902 eV. This is because in the supercell the interatomic bonds in PbSe layer are smaller than those in the equilibrium PbSe bulk phase. The substrate lattice parameter is 1.2% smaller than that of

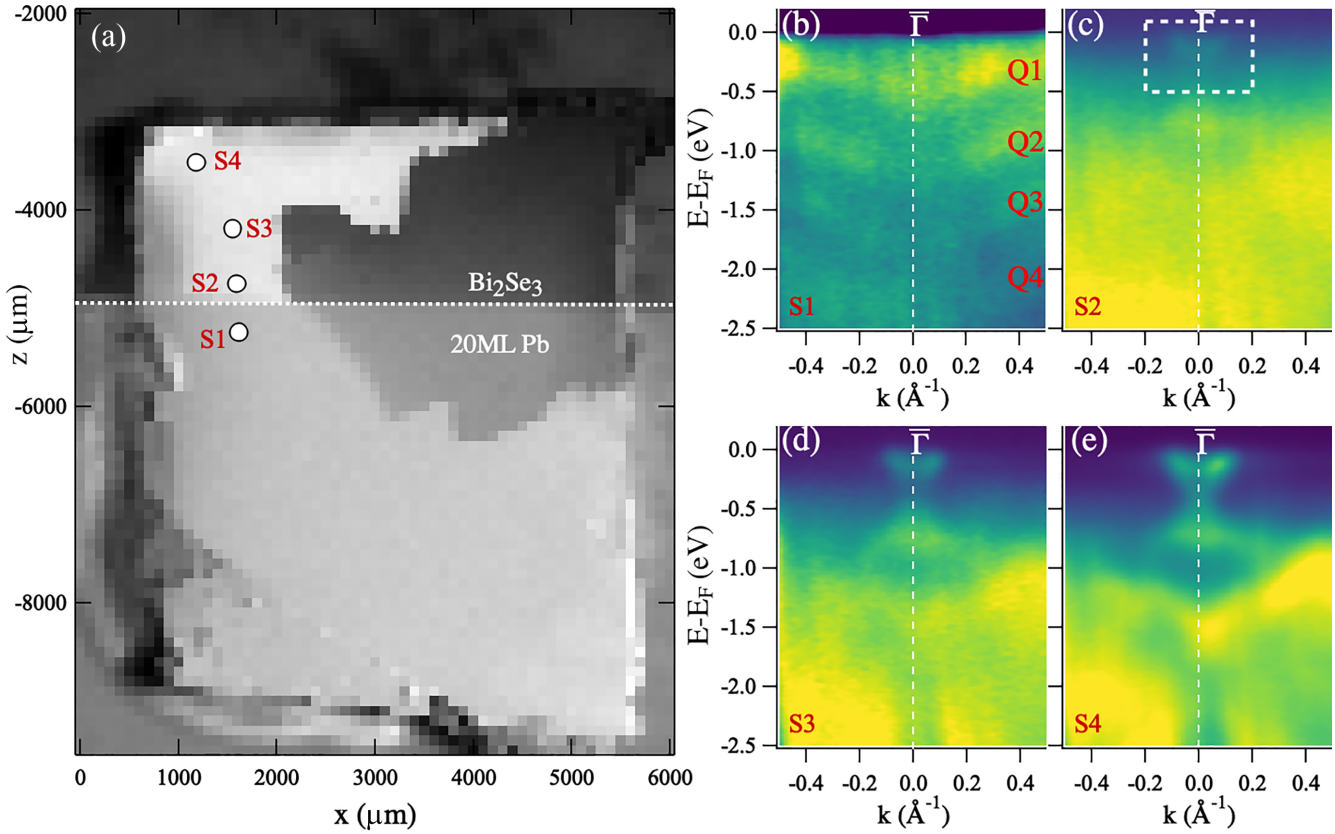

FIG. 5. (a) SPEM intensity map of the investigated Bi_2Se_3 acquired with 74 eV photon energy. The dotted line marks the edge of the 20 ML Pb film. (b)–(e) μ-ARPES band structure recorded with 74 eV photon energy collected at the sample spots labeled S1-S4 in (a). Q1-Q4 in (b) mark the quantum well states of Pb. In (c), the TSS is highlighted by a white dotted rectangle.

PbSe(111). The pressure in the cubic PbSe phase, calculated with parameters corresponding to the compression provided by the substrate, is 21 kbar. Therefore, the nucleus of the PbSe phase cannot attain a considerable size.

Thus, according to our simulations, as a result of the energetically favorable surface rearrangement caused by lead deposition, clusters of PbSe phase will be formed on the surface. The size of these clusters is limited by the stresses induced by the substrate. Between the PbSe phase nucleus, there should also be regions in the surface where displaced bismuth atoms will be located. It is important to note that the present simulation of PbSe-phase nucleation, limited by the relatively small supercell size, does not include the presence of thallium islands on the surface. Although Tl islands may locally perturb Pb deposition on Se-terminated regions, our *ab initio* calculations and μ-PES measurements indicate a negligible Pb–Tl interaction, suggesting that Pb–Se interactions dominate the nucleation of PbSe clusters. Furthermore, explicitly incorporating Tl islands into the simulations would require a substantial increase in the supercell size. We have shown at the beginning that isolated Pb adsorbates are expected to avoid Tl islands. Previous experiments have shown that Tl islands are typically small ($\sim$10 atoms and smaller [54]).

As the inhomogeneities at the selenium termination increase, which is associated with the formation of PbSe nuclei, the mobility of thallium is expected to diminish, and the thallium islands will be forced to coalesce. Therefore, the complete picture of the initial stage of lead adsorption should encompass the coexistence of unevenly distributed, coarse thallium islands, small nuclei of the PbSe phase, and metallic bismuth islands, formed by Bi atoms that segregated to the surface, potentially alongside areas where initial selenium termination do not engage with the adsorbed lead atoms.

B. Pb/Bi_2Se_3

The crystal structure of $TlBiSe_2$ differs significantly from that of the binary-layered compound Bi_2Se_3. In Bi_2Se_3, cleavage occurs between van der Waals-coupled quintuple layers, and wide clean and ordered surfaces can be created. The topmost layers composed of Se terraces of the two systems coincide, apart from the highly mobile thallium atoms.

To investigate whether the formation of a Pb-induced disordered interface is peculiar to $TlBiSe_2$, a mask was used to selectively deposit 20 ML of Pb on one side only of a Bi_2Se_3 surface. In Fig. 5(a) we report the SPEM intensity image of the investigated sample which allows us to discern the portion of the Bi_2Se_3 surface covered by the Pb film from the pristine surface. A dark zone is also observed in the top-right region due to an uncleaved portion of the sample. Several spots of the sample were examined using μ-ARPES and μ-PES to study the corresponding electronic structure—here we report four of them labeled S1–S4 in Fig. 5(a).

Figure 5(b) displays a representative μ-ARPES spectrum collected in the surface region covered by 20 ML of Pb (spot S1). The band structure in this region reveals at least four Pb

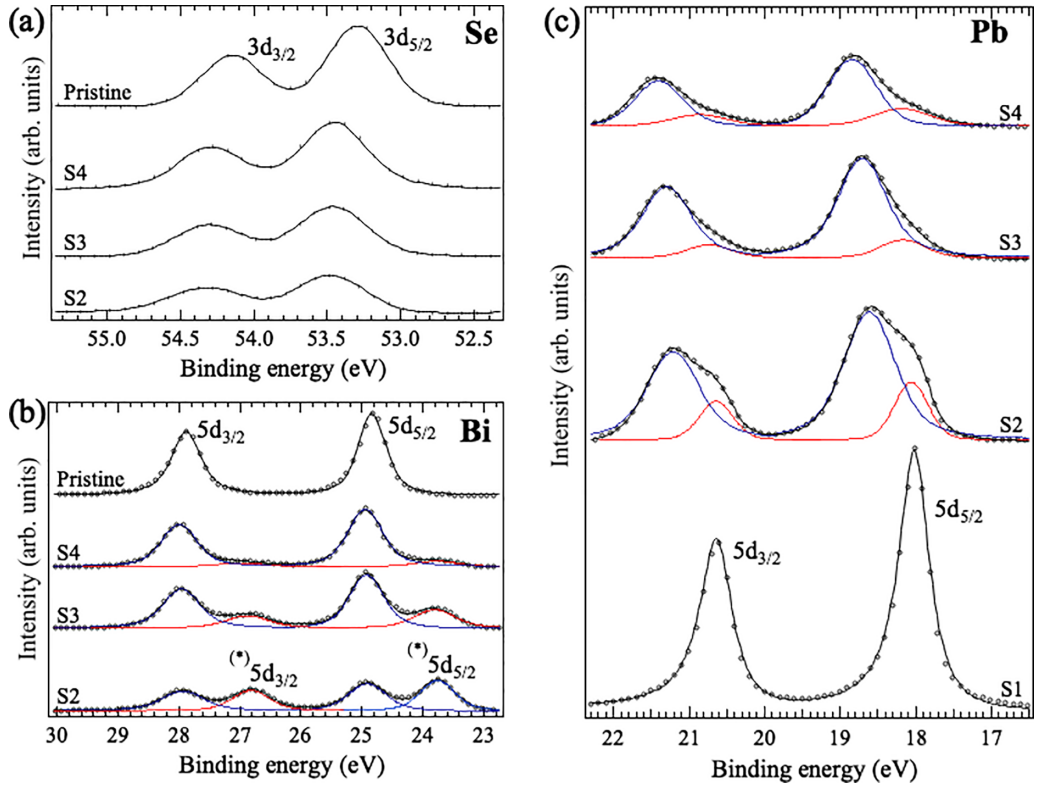

FIG. 6. Photoemission spectra for (a) Se 3*d*, (b) Bi 5*d*, and (c) Pb 5*d* core levels collected from the sample regions labeled S1–S4 in Fig. 5(a). In (a) and (b), the Se 3*d* and Bi 5*d* for pristine Bi_2Se_3 are also included. The intensities of the core states have been rescaled to facilitate the comparison between regions.

QWs (labeled Q1–Q4), indicating the formation of a relatively thick Pb film. Under these experimental conditions, no TSS or electronic features related to the Bi_2Se_3 substrate were observed, in agreement with earlier results [30].

Figure 5(c) presents μ-ARPES measurements collected at point S2, near the edge of the 20 ML Pb film. The amount of Pb in this region, due to Pb atoms diffusion at LN temperature, is estimated to be around 1 ML [30]. Here, the electronic states of Bi_2Se_3 appear diffuse and blurry, with the TSS of the substrate barely detectable [highlighted by a white dotted rectangle in Fig. 5(c)]. As sample regions away from the edge of the 20 ML Pb film are probed, the electronic structure of Bi_2Se_3 becomes clearer. In Fig. 5(d), recorded from S3 point (Pb coverage < 1 ML), the band structure of Bi_2Se_3 is more refined, while at S4 (the region farthest from the Pb film), the pristine electronic structure is partially recovered, as shown in Fig. 5(e). A closer inspection, however, reveals modifications of the valence-band electronic structure with respect to the pristine sample (see Fig. 12). These results are in agreement with earlier photoemission measurements on Pb/Bi_2Se_3 [30], which showed that the TSS persists only weakly up to Pb coverages of approximately 1 ML and disappears at higher coverages. Here we show that, on the submonolayer Pb regime, the perturbation of the TSS increases with the increasing amount of Pb atoms at the surface.

Figure 6 displays the photoemission from core levels collected on the same sample spots investigated by μ-ARPES. Figures 6(a) and 6(b) include the Se and Bi core states (labeled "pristine"), measured before Pb deposition. It is evident that the photoemission intensity of the Se 3*d* core states increases as one moves away from the edge of the 20 ML Pb film. Apart from the intensity change, Se 3*d* binding energies, centered at 54.34 and 53.48 eV, remain nearly unchanged in the S2-S4 regions, with a constant shift of ∼150 meV toward a higher binding energy as compared to the pristine sample.

Similarly to $TlBiSe_2$, the most significant differences in the core level states are observed in the Bi 5*d* states. For pristine Bi_2Se_3, the Bi $5d_{3/2}$ and $5d_{5/2}$ states centered at 27.87 and 24.83 eV shift to higher binding energies by ∼100 meV in the S2-S4 regions [30]. More importantly, two additional features corresponding to metallic Bi [labeled as $^{(*)}5d$ in Fig. 6(b)] are detected at 26.78 and 23.72 eV whose intensity decreases with distance from the edge of the Pb film.

The Pb-Bi_2Se_3 interaction is also evidenced in Fig. 6(c), showing the Pb 5*d* states. Two main components are observed at 20.65 and 18.02 eV for the 20 ML thick Pb film, ascribed to $5d_{3/2}$ and $5d_{5/2}$ bulk states, respectively. As sample regions

TABLE I. Summary of notable energy values calculated for Pb on $TlBiSe_2$ and Bi_2Se_3 substrates. Highlighted in bold is the difference in the energy gain for the Pb-Bi swapping, in the case of a large cluster.

	$TlBiSe_2$	Bi_2Se_3
Pb-Bi swapping/single atom (eV)	+0.715	+0.203
Pb-Bi swapping/cluster (eV)	**–0.363**	**–1.159**
PbSe cluster compression (kbar)	21	98

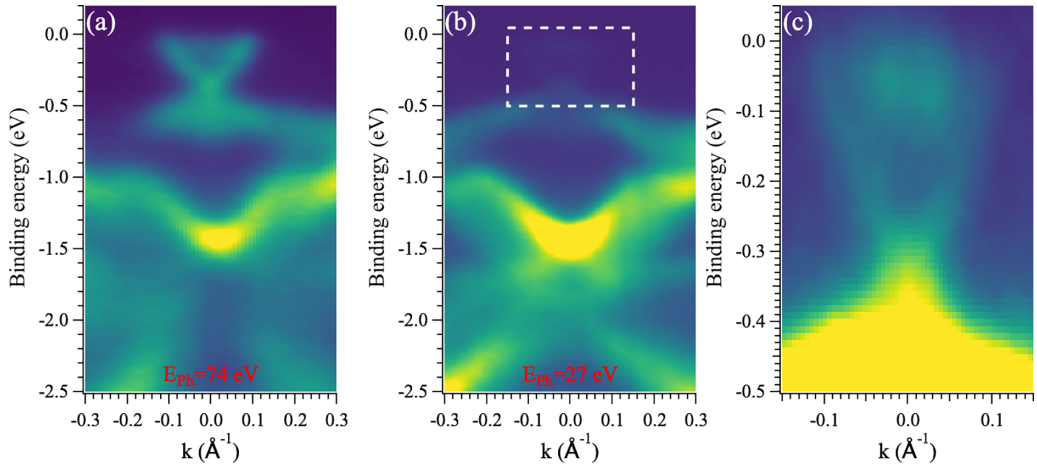

FIG. 7. ARPES intensity maps collected on Bi_2Se_3 using photon energies of (a) 74 eV and (b) 27 eV. (c) Magnified view of the white dotted rectangle in (b).

away the 20 ML Pb film are probed, changes in the intensity and line shape of the Pb 5*d* states become evident. Specifically, bulk-related features lose intensity, and new components emerge, shifted by 600 meV toward a higher binding energy, attributed to reacted Pb. These states exhibit a ∼200 meV shift toward a higher binding energy, moving from the S2 to the S4 region.

These measurements indeed prove high mobility (of the order of *mm*) of Pb atoms at LN temperature. Furthermore, the μ-ARPES and μ-PES results on Pb/Bi_2Se_3 strongly suggest that the interaction between Pb and Bi_2Se_3 is similar to that observed for $Pb/TlBiSe_2$. Having carried out calculations for Pb/Bi_2Se_3 interactions similar to those discussed in detail above for the Se termination of $TlBiSe_2$, we also found that swapping a single Pb adsorbate with $Bi_{(2)}$ atoms is not profitable. However, the swapping energy is significantly lower, +0.203 eV, compared to the previous case (+0.715 eV). In the case of a lead monolayer (an extended Pb island) on the surface, as in the previous case, swapping of Pb-Bi pair becomes energetically favorable, which initiates the PbSe phase formation. However, again, while in the case of $TlBiSe_2$ such swapping provided an energy gain of 0.363 eV, on the surface of bismuth selenide this swapping of a single Pb-Bi pair is more favorable, $\Delta E = -1.159$ eV, see Table. I. This indicates that the substitution of bismuth by lead with the simultaneous migration of bismuth on the surface in Bi_2Se_3 occurs more actively compared to $TlBiSe_2$. On the other hand, the lattice parameter of Bi_2Se_3 is smaller than that of $TlBiSe_2$ and, therefore, the growing nuclei of the PbSe phase should experience larger stress. The pressure in the PbSe, calculated with parameters corresponding to the compression provided by the Bi_2Se_3 substrate, is about 5 times larger, 98 kbar and hence the PbSe nucleus should be smaller than on the $TlBiSe_2$ surface.

It is noted that the above theoretical prediction is consistent with the experimental results: the lower the amount of lead (zone S4), the lower the swapping probability, the smaller the intensity of the Bi metallic component (related to the segregated Bi atoms). Moving toward the 20 ML Pb step (S2) at variance, the amount of segregated bismuth increases. The evolution of the Bi metallic peak then closely follows the relation between the amount of lead atoms deposited and the softening of the $Se_{(3)} - Bi_{(2)}$ bond, inducing the atom swapping.

IV. CONCLUSIONS

In this study, we performed a surface-sensitive and spatially resolved photoemission investigation of the electronic structure of Pb films grown on the topological insulators $TlBiSe_2$ and Bi_2Se_3. μ-ARPES results on $Pb/TlBiSe_2$ heterostructures reveal that the initial Pb deposition, at 2 ML coverage, leads to the formation of a highly disordered interface characterized by the complete disappearance of the $TlBiSe_2$ topological surface state. This interface is found to consist of an intermixing phase where the pristine crystal coexists with Pb-Se nuclei and Pb islands, as supported by the angle-resolved valence band and by the photoemission analysis of the Pb 5*d* and Se 3*d* core levels. For thicker Pb films on both $TlBiSe_2$ and Bi_2Se_3, well-defined QW states are observed, confirming the formation of crystalline Pb layers following a Stranski-Krastanov growth mode; however, no migration of the TSS onto the Pb film surface could be detected under our experimental conditions.

Core-level photoemission data on both $Pb/TlBiSe_2$ and Pb/Bi_2Se_3 consistently point to a strong interaction between Pb and the Se atoms of the substrate. This Pb-Se bond formation induces the migration toward the surface of Bi atoms, resulting in the appearance of a metallic Bi phase at the surface. This chemical degradation of the substrate's topmost layers disrupts the structural integrity required for the TSS to propagate, acting as a scattering mechanism that hinders or destroys the TSS before it can effectively couple with the Pb overlayer. Spatially-resolved measurements on the Pb/Bi_2Se_3 system show that the Pb-induced degradation effects, including the formation of metallic Bi, can extend laterally far beyond the immediate boundary of the Pb film, highlighting a relevant mobility of Pb atoms at LN temperature and suggesting a Pb-driven surface intermixing process.

The DFT simulation was performed, encompassing calculations of the total energies, identification of the preferred adsorption sites. Additionally, interatomic chemical bond strengths were calculated using the COHP analysis for ideal

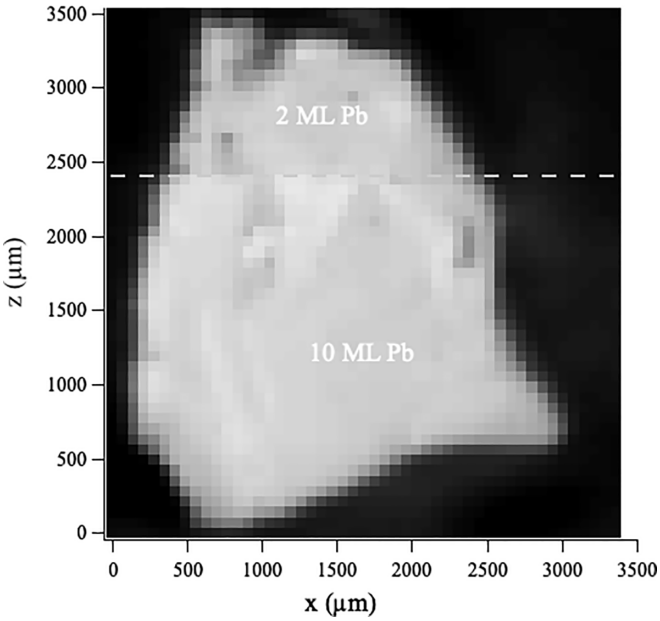

FIG. 8. SPEM image of the investigated Pb/$TlBiSe_2$ system recorded on the Pb $5d_{5/2}$ states at 18 eV binding energy. The dotted line marks the edge between the 2 ML and 10 ML Pb film.

surfaces with single atoms, with adsorbate islands and surfaces undergoing the adsorbate-substrate swapping. This modeling demonstrated that for single Pb adatoms, the Pb-Se bond energies are so strong that they prevent the surface reactions. When Pb islands increase in size, Pb-Bi swapping becomes favorable, leading to the formation of PbSe nuclei, and

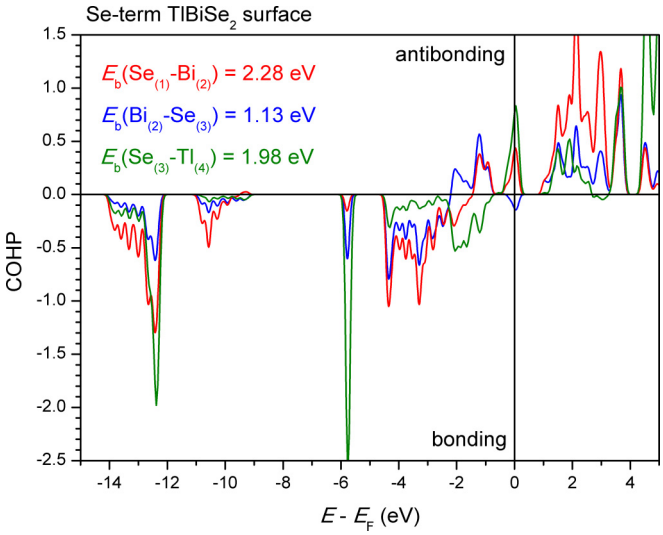

FIG. 9. Crystal orbital Hamilton population (COHP) for bonds between neighboring atoms of the first and second ($Se_{(1)}$-$Bi_{(2)}$, red line), second and third ($Bi_{(2)}$-$Se_{(3)}$, blue line), and third and fourth ($Se_{(3)}$-$Tl_{(4)}$, green line) layers of Se-terminated $TlBiSe_2$ surface. Positive (negative) sign of COHP corresponds to antibonding (bonding) interaction. Interatomic bond energies (E_b), as extracted from integration of the COHP below E_F, show the strength of the bond between bismuth and the third layer Se atoms is approximately one eV lower than that between it and selenium of the topmost layer. This is because $Se_{(3)}$ interacts strongly with $Tl_{(4)}$.

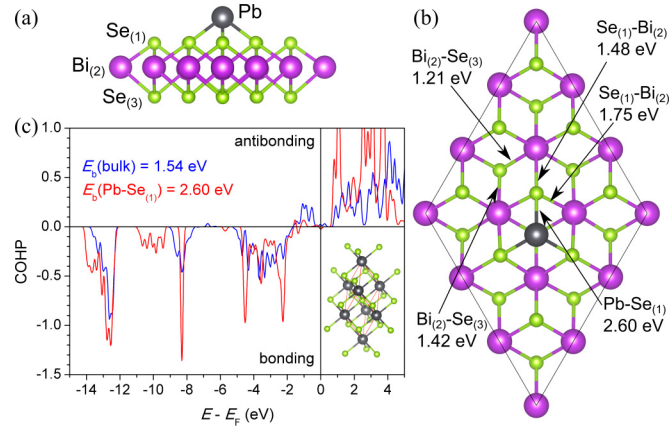

FIG. 10. Side (a) and top (b) views of the Se-terminated $TlBiSe_2$ surface with single Pb adatom at preferred fcc adsorption position (H-passivated Tl layer is not shown). The bonds between adsorbed Pb and neighboring Se atoms are strong. They are more than 1 eV stronger than bonds in cubic PbSe bulk phase (c). Inset in (c) shows atomic structure of the primitive cell of cubic PbSe. The energies of bonds between near-surface atoms are no longer equivalent like on the clean Se termination but depend on the Se-Bi pair position relative to the Pb adatom. As can be seen in (b), overall, the $Se_{(1)}$-$Bi_{(2)}$ bonds are significantly weakened, while the Bi_2-Se_3 bonds are slightly strengthened compared to the clean Se termination (see Fig. 9). Moreover, larger weakening of the Se-Bi bonds is observed for the second-nearest Bi neighbors of the adatom.

to substantial decrease of the Se-Bi bond energies while Se-Pb bond energies become comparable to those in the cubic PbSe bulk phase. The size of PbSe nuclei is limited by the compressive stresses exerted by the TI substrate. Thus, our modeling corroborates the experimental findings, indicating a significant surface degradation caused by the development of a disordered layer, which is realized through the formation of PbSe phase nuclei and the segregation of bismuth onto the surface.

ACKNOWLEDGMENTS

This research was partially supported by Progetto STAR 2 (PIR01-00008) of the Italian Ministry of Education, University, and Research (MUR). S.V.E. appreciates A.V. Bakulin for valuable discussions and acknowledges support from the government research assignment for ISPMS SB RAS, Project No. FWRW-2026-0008. A.G.R. acknowledges support from the government research assignment for ISP SB RAS, Project No. FWRW-2025-0014. E.V.C. acknowledges Saint-Petersburg State University for research Project No. 125022702939-2. The calculations were partly conducted using the equipment of the Shared Resource Center Far Eastern Computing Resource IACP FEB RAS [74] and Computational Center of Novosibirsk State University [75] .

DATA AVAILABILITY

The data that support the findings of this article are not publicly available upon publication because it is not techni-

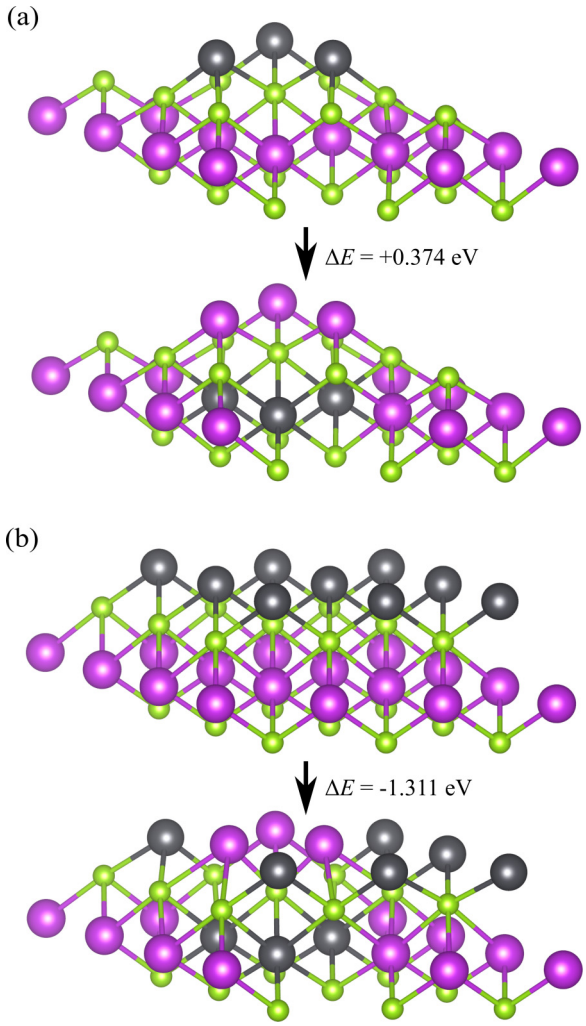

FIG. 11. Swapping of three Pb-Bi pairs in cases of Pb trimer on Se termination (a) and Pb monolayer (b).

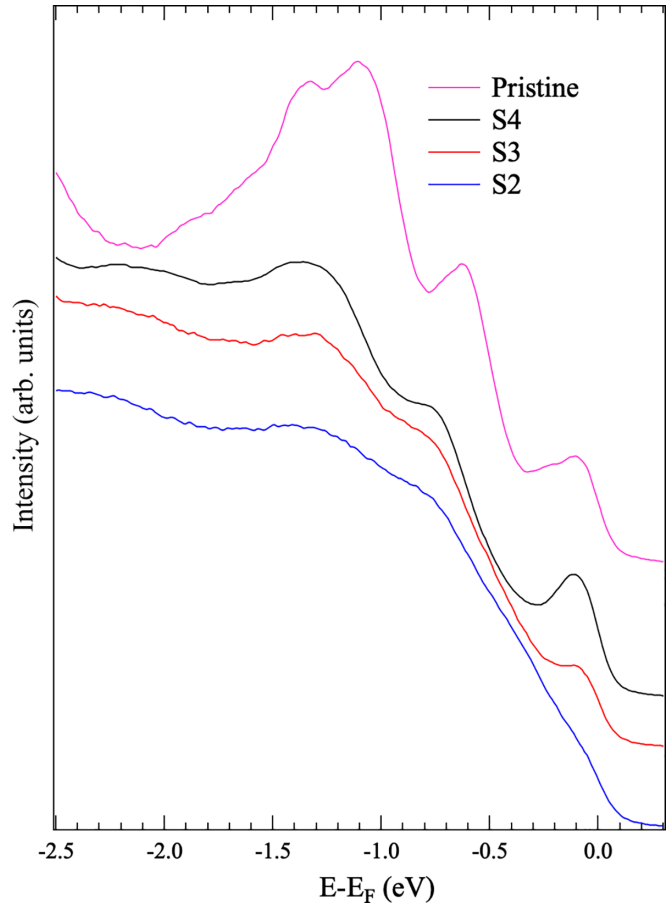

FIG. 12. Valence band extracted from Figs. 5(c)–5(e) along with the spectrum of pristine Bi_2Se_3.

cally feasible and/or the cost of preparing, depositing, and hosting the data would be prohibitive within the terms of this research project. The data are available from the authors upon reasonable request.

APPENDIX: ADDITIONAL FIGURES

Figures 7(a) and 7(b) display the μ-ARPES band structure of pristine Bi_2Se_3 measured using photon energies of 74 and 27 eV, respectively. (c) Zoom-in of the region enclosed by the white dotted rectangle in (b), highlighting the topological surface state. Figure 8 shows the SPEM intensity map of $TlBiSe_2$ covered with 2 ML and 5 ML Pb film. Figure 9 reports the COHP analysis for the interatomic bonds on the Se-terminated $TlBiSe_2$ surface, evidencing a substantially weaker interaction between second layer Bi atoms and third layer Se atoms compared to surface Se. Figures 10 shows the evolution of local Se-Bi bonds on the Se-terminated $TlBiSe_2$ surface in the presence of a single lead adsorbate and a comparison of Pb-Se bonds on the surface with bonds in the cubic PbSe bulk phase. Figure 11 displays a sketch of the swapping of three Pb-Bi pairs in cases of Pb trimer on Se termination (a) and Pb monolayer (b). Figure 12 displays the valence-band spectra of pristine Bi_2Se_3 (magenta curve) and of the regions labeled S2–S4 in Fig. 5 (blue, red, and black curves, respectively).

[1] B. A. Bernevig, T. L. Hughes, and S.-C. Zhang, Quantum spin Hall effect and topological phase transition in HgTe quantum wells, Science **314**, 1757 (2006).

[2] J. Biscaras, N. Bergeal, A. Kushwaha, T. Wolf, A. Rastogi, and J. Lesueur, Two-dimensional superconductivity at a Mott insulator/band insulator interface $LaTiO_3/SrTiO_3$, Nat. Commun. **89**, 1 (2010).

[3] D. Delagebeaudeuf and N. Linh, Metal-(n) AlGaAs-GaAs two-dimensional electron gas FET, IEEE Trans. Electron Devices **29**, 955 (1982).

[4] Y. Cao, V. Fatemi, S. Fang, K. Watanabe, T. Taniguchi, E. Kaxiras, and P. Jarillo-Herrero, Unconventional superconductivity in magic-angle graphene superlattices, Nature (London) **556**, 43 (2018).

[5] S. Nadj-Perge, I. K. Drozdov, J. Li, H. Chen, S. Jeon, J. Seo, A. H. MacDonald, B. A. Bernevig, and A. Yazdani, Observation of Majorana fermions in ferromagnetic atomic chains on a superconductor, Science **346**, 602 (2014).

[6] K. Holtgrewe, S. K. Mahatha, P. M. Sheverdyaeva, P. Moras, R. Flammini, S. Colonna, F. Ronci, M. Papagno, A. Barla, L. Petaccia, Z. S. Aliev, M. B. Babanly, E. V. Chulkov, S. Sanna, C. Hogan, and C. Carbone, Topologization of β-antimonene on Bi_2Se_3 via proximity effects, Sci. Rep. **10**, 14619 (2020).

[7] H. le Sueur, P. Joyez, H. Pothier, C. Urbina, and D. Esteve, Phase controlled superconducting proximity effect probed by tunneling spectroscopy, Phys. Rev. Lett. **100**, 197002 (2008).

[8] F. Giazotto, J. T. Peltonen, M. Meschke, and J. P. Pekola, Superconducting quantum interference proximity transistor, Nat. Phys. **6**, 254 (2010).

[9] Z. Wang, C. Tang, R. Sachs, Y. Barlas, and J. Shi, Proximity-induced ferromagnetism in graphene revealed by the anomalous Hall effect, Phys. Rev. Lett. **114**, 016603 (2015).

[10] X.-Y. Ren, H.-J. Kim, S. Yi, Y. Jia, and J.-H. Cho, Spin-orbit coupling effects on the stability of two competing structures in Pb/Si(111) and Pb/Ge(111), Phys. Rev. B **94**, 075436 (2016).

[11] C. Brand, S. Muff, M. Fanciulli, H. Pfnür, M. C. Tringides, J. H. Dil, and C. Tegenkamp, Spin-resolved band structure of a densely packed Pb monolayer on Si(111), Phys. Rev. B **96**, 035432 (2017).

[12] L. Fu and C. L. Kane, Superconducting proximity effect and Majorana fermions at the surface of a topological insulator, Phys. Rev. Lett. **100**, 096407 (2008).

[13] F. Qu, F. Yang, J. Shen, Y. Ding, J. Chen, Z. Ji, G. Liu, J. Fan, X. Jing, C. Yang, and L. Lu, Strong superconducting proximity effect in Pb-Bi_2Te_3 hybrid structures, Scientific Report **2**, 5 (2012).

[14] S. Charpentier, G. Kunakova, R. Arpaia, Y. Song, R. Baghdadi, S. M. Wang, A. Kalaboukhov, E. Olsson, F. Tafuri, D. Golubev, J. Linder, T. Bauch, and F. Lombardi, Induced unconventional superconductivity on the surface states of Bi_2Te_3 topological insulator, Nat. Commun. **8**, 2019 (2019).

[15] L. Fu, C. L. Kane, and E. J. Mele, Topological insulators in three dimensions, Phys. Rev. Lett. **98**, 106803 (2007).

[16] C. L. Kane and E. J. Mele, Z_2 topological order and the quantum spin Hall effect, Phys. Rev. Lett. **95**, 146802 (2005).

[17] M. Z. Hasan and C. L. Kane, *Colloquium*: Topological insulators, Rev. Mod. Phys. **82**, 3045 (2010).

[18] D. Pacilè, S. V. Eremeev, M. Caputo, M. Pisarra, O. De Luca, I. Grimaldi, J. Fujii, Z. S. Aliev, M. B. Babanly, I. Vobornik, R. G. Agostino, A. Goldoni, E. V. Chulkov, and M. Papagno, Deep insight into the electronic structure of ternary topological insulators: A comparative study of $PbBi_4Te_7$ and $PbBi_6Te_{10}$, Phys. Rapid Res. Ltrs **12**, 1800341 (2018).

[19] C. Liu and J.-F. Jia, Creating Majorana fermions in topological insulators, Natl. Sci. Rev. **1**, 36 (2014).

[20] J.-P. Xu, M.-X. Wang, Z. L. Liu, J.-F. Ge, X. Yang, C. Liu, Z. A. Xu, D. Guan, C. L. Gao, D. Qian, Y. Liu, Q.-H. Wang, F.-C. Zhang, Q.-K. Xue, and J.-F. Jia, Experimental detection of a Majorana mode in the core of a magnetic vortex inside a topological insulator-superconductor $Bi_2Te_3/NbSe_2$ heterostructure, Phys. Rev. Lett. **114**, 017001 (2015).

[21] K. Miyamoto, A. Kimura, T. Okuda, H. Miyahara, K. Kuroda, H. Namatame, M. Taniguchi, S. V. Eremeev, T. V. Menshchikova, E. V. Chulkov, K. A. Kokh, and O. E. Tereshchenko, Topological surface states with persistent high spin polarization across the Dirac point in Bi_2Te_2Se and Bi_2Se_2Te, Phys. Rev. Lett. **109**, 166802 (2012).

[22] C. Beenakker, Search for Majorana fermions in superconductors, Annu. Rev. Condens. Matter Phys. **4**, 113 (2013).

[23] H. Zhang, C.-X. Liu, X.-L. Qi, X. Dai, Z. Fang, and S.-C. Zhang, Topological insulators in Bi_2Se_3, Bi_2Te_3 and Sb_2Te_3 with a single Dirac cone on the surface, Nat. Phys. **5**, 438 (2009).

[24] C. X. Trang, N. Shimamura, K. Nakayama, S. Souma, K. Sugawara, I. Watanabe, K. Yamauchi, T. Oguchi, K. Segawa, T. Takahashi, Y. Ando, and T. Sato, Conversion of a conventional superconductor into a topological superconductor by topological proximity effect, Nat. Commun. **11**, 159 (2020).

[25] C. Brun, I.-P. Hong, F. Patthey, I. Y. Sklyadneva, R. Heid, P. M. Echenique, K. P. Bohnen, E. V. Chulkov, and W.-D. Schneider, Reduction of the superconducting gap of ultrathin Pb islands grown on Si(111), Phys. Rev. Lett. **102**, 207002 (2009).

[26] L. Serrier-Garcia, J. C. Cuevas, T. Cren, C. Brun, V. Cherkez, F. Debontridder, D. Fokin, F. S. Bergeret, and D. Roditchev, Scanning tunneling spectroscopy study of the proximity effect in a disordered two-dimensional metal, Phys. Rev. Lett. **110**, 157003 (2013).

[27] S. Xu, N. Alidoust, I. Belopolski, A. Richardella, C. Liu, M. Neupane, G. Bian, S. Huang, R. Sankar, C. Fang, B. Dellabetta, W. Dai, Q. Li, M. J. Gilbert, F. Chou, N. Samarth, and M. Z. Hasan, Momentum-space imaging of Cooper pairing in a half-Dirac-gas topological superconductor, Nat. Phys. **10**, 943 (2014).

[28] K. Nakayama, H. Kimizuka, Y. Tanaka, T. Sato, S. Souma, T. Takahashi, S. Sasaki, K. Segawa, and Y. Ando, Observation of two-dimensional bulk electronic states in the superconducting topological insulator heterostructure $Cu_x(PbSe)_5(Bi_2Se_3)_6$: Implications for unconventional superconductivity, Phys. Rev. B **92**, 100508(R) (2015).

[29] Y. Li, Y.-h. Chan, J. A. Hlevyack, J. W. Bowers, M.-Y. Chou, and T.-C. Chiang, Topological quantum well states in Pb/Sb thin-film heterostructures, ACS Nano **18**, 10243 (2024).

[30] O. De Luca, I. A. Shvets, S. V. Eremeev, Z. S. Aliev, M. Kopciuszynski, A. Barinov, F. Ronci, S. Colonna, E. V. Chulkov, R. G. Agostino, M. Papagno, and R. Flammini, Floating of the topological surface state on top of a thick lead layer: The case of the Pb/Bi_2Se_3 interface, Phys. Rev. Mater. **7**, 124203 (2023).

[31] P. Dudin, P. Lacovig, C. Fava, E. Nicolini, A. Bianco, G. Cautero, and A. Barinov, Angle-resolved photoemission spectroscopy and imaging with a submicrometre probe at the SPECTROMICROSCOPY-3.2L beamline of Elettra, J. Synchrotron Radiat. **17**, 445 (2010).

[32] P. E. Blöchl, Projector augmented-wave method, Phys. Rev. B **50**, 17953 (1994).

[33] G. Kresse and J. Furthmüller, Efficient iterative schemes for *ab initio* total-energy calculations using a plane-wave basis set, Phys. Rev. B **54**, 11169 (1996).

[34] G. Kresse and D. Joubert, From ultrasoft pseudopotentials to the projector augmented-wave method, Phys. Rev. B **59**, 1758 (1999).

[35] J. P. Perdew, K. Burke, and M. Ernzerhof, Generalized gradient approximation made simple, Phys. Rev. Lett. **77**, 3865 (1996).

[36] S. Grimme, S. Ehrlich, and L. Goerigk, Effect of the damping function in dispersion corrected density functional theory, J. Comput. Chem. **32**, 1456 (2011).

[37] K. Hoang and S. D. Mahanti, Atomic and electronic structures of thallium-based III-V-VI_2 ternary chalcogenides: *Ab initio* calculations, Phys. Rev. B **77**, 205107 (2008).

[38] R. Dronskowski and P. E. Bloechl, Crystal orbital Hamilton populations (COHP): Energy-resolved visualization of chemical bonding in solids based on density-functional calculations, J. Phys. Chem. **97**, 8617 (1993).

[39] V. L. Deringer, A. L. Tchougréeff, and R. Dronskowski, Crystal orbital Hamilton population (COHP) analysis as projected from plane-wave basis sets, J. Phys. Chem. A **115**, 5461 (2011).

[40] S. Maintz, V. L. Deringer, A. L. Tchougréeff, and R. Dronskowski, LOBSTER: A tool to extract chemical bonding from plane-wave based DFT, J. Comput. Chem. **37**, 1030 (2016).

[41] K. Kuroda, M. Ye, A. Kimura, S. V. Eremeev, E. E. Krasovskii, E. V. Chulkov, Y. Ueda, K. Miyamoto, T. Okuda, K. Shimada, H. Namatame, and M. Taniguchi, Experimental realization of a three-dimensional topological insulator phase in ternary chalcogenide $TlBiSe_2$, Phys. Rev. Lett. **105**, 146801 (2010).

[42] T. Sato, K. Segawa, H. Guo, K. Sugawara, S. Souma, T. Takahashi, and Y. Ando, Direct evidence for the Dirac-cone topological surface states in the ternary chalcogenide $TlBiSe_2$, Phys. Rev. Lett. **105**, 136802 (2010).

[43] H. Lin, R. S. Markiewicz, L. A. Wray, L. Fu, M. Z. Hasan, and A. Bansil, Single-Dirac-cone topological surface states in the $TlBiSe_2$ class of topological semiconductors, Phys. Rev. Lett. **105**, 036404 (2010).

[44] B. Yan, C.-X. Liu, H.-J. Zhang, C.-Y. Yam, X.-L. Qi, T. Frauenheim, and S.-C. Zhang, Theoretical prediction of topological insulators in thallium-based III-V-VI_2 ternary chalcogenides, Europhys. Lett. **90**, 37002 (2010).

[45] S. V. Eremeev, G. Bihlmayer, M. Vergniory, Y. M. Koroteev, T. V. Menshikova, J. Henk, A. Ernst, and E. V. Chulkov, *Ab initio* electronic structure of thallium-based topological insulators, Phys. Rev. B **83**, 205129 (2011).

[46] I. I. Klimovskikh, D. A. Estyunin, T. P. Makarova, O. E. Tereshchenko, K. A. Kokh, and A. M. Shikin, Electronic structure of Pb adsorbed surfaces of intrinsic magnetic topological insulators, J. Phys. Chem. Lett. **13**, 6628 (2022).

[47] D. A. Estyunin, T. P. Makarova, K. A. Kokh, O. E. Tereshchenko, A. M. Shikin, and I. I. Klimovskikh, Contact of the intrinsic magnetic topological insulator $Mn(Bi, Sb)_2Te_4$ with a superconducting Pb film, Phys. Rev. B **106**, 155305 (2022).

[48] K. Horn, B. Reihl, A. Zartner, D. E. Eastman, K. Hermann, and J. Noffke, Electronic energy bands of lead: Angle-resolved photoemission and band-structure calculations, Phys. Rev. B **30**, 1711 (1984).

[49] A. Mans, J. H. Dil, A. R. H. F. Ettema, and H. H. Weitering, Quantum electronic stability and spectroscopy of ultrathin Pb films on Si(111)7 × 7, Phys. Rev. B **66**, 195410 (2002).

[50] C. M. Wei and M. Y. Chou, Theory of quantum size effects in thin Pb(111) films, Phys. Rev. B **66**, 233408 (2002).

[51] M. H. Upton, T. Miller, and T.-C. Chiang, Unusual band dispersion in Pb films on Si(111), Phys. Rev. B **71**, 033403 (2005).

[52] J. H. Dil, T. U. Kampen, B. Hülsen, T. Seyller, and K. Horn, Quantum size effects in quasi-free-standing Pb layers, Phys. Rev. B **75**, 161401(R) (2007).

[53] B. Slomski, G. Landolt, S. Muff, F. Meier, J. Osterwalder, and J. H. Dil, Interband spin-orbit coupling between anti-parallel spin states in Pb quantum well states, New J. Phys. **15**, 125031 (2013).

[54] K. Kuroda, M. Ye, E. F. Schwier, M. Nurmamat, K. Shirai, M. Nakatake, S. Ueda, K. Miyamoto, T. Okuda, H. Namatame, M. Taniguchi, Y. Ueda, and A. Kimura, Experimental verification of the surface termination in the topological insulator $TlBiSe_2$ using core-level photoelectron spectroscopy and scanning tunneling microscopy, Phys. Rev. B **88**, 245308 (2013).

[55] J. C. Fuggle and N. Mårtensson, Core-level binding energies in metals, J. Electron Spectrosc. Relat. Phenom. **21**, 275 (1980).

[56] L. A. Walsh, C. M. Smyth, A. T. Barton, Q. Wang, Z. Che, R. Yue, J. Kim, M. J. Kim, R. M. Wallace, and C. L. Hinkle, Interface chemistry of contact metals and ferromagnets on the topological insulator Bi_2Se_3, J. Phys. Chem. C **121**, 23551 (2017).

[57] Y. A. Surnin, I. I. Klimovskikh, D. M. Sostina, K. A. Kokh, O. E. Tereshchenko, and A. M. Shikin, Impact of ultrathin Pb films on the topological surface and quantum-well states of Bi_2Se_3 and Sb_2Te_3 topological insulators, J. Exp. Theor. Phys. **126**, 535 (2018).

[58] M. Fanetti, I. Mikulska, K. Ferfolja, P. Moras, P. Sheverdyaeva, M. Panighel, A. Lodi-Rizzini, I. Pis, S. Nappini, M. Valant, and S. Gardonio, Growth, morphology and stability of Au in contact with the Bi_2Se_3(0001) surface, Appl. Surf. Sci. **471**, 753 (2019).

[59] N. de Jong, E. Frantzeskakis, B. Zwartsenberg, Y. K. Huang, D. Wu, P. Hlawenka, J. Sańchez-Barriga, A. Varykhalov, E. van Heumen, and M. S. Golden, Angle-resolved and core-level photoemission study of interfacing the topological insulator $Bi_{1.5}Sb_{0.5}Te_{1.7}Se_{1.3}$ with Ag, Nb, and Fe, Phys. Rev. B **92**, 075127 (2015).

[60] Å. Olin, B. Noläng, L. O. Öhman, E. Osadchii, and E. Rosén, Chemical thermodynamics of selenium, Elsevier Science: Amsterdam **7** (2005).

[61] I. Vobornik, G. Panaccione, J. Fujii, Z.-H. Zhu, F. Offi, B. R. Salles, F. Borgatti, P. Torelli, J. P. Rueff, D. Ceolin, A. Artioli, M. Unnikrishnan, G. Levy, M. Marangolo, M. Eddrief, D. Krizmancic, H. Ji, A. Damascelli, G. van der Laan, R. G. Egdell, *et al.*, Observation of distinct bulk and surface chemical environments in a topological insulator under magnetic doping, J. Phys. Chem. C **118**, 12333 (2014).

[62] E. Wang, P. Tang, G. Wan, A. V. Fedorov, I. Miotkowski, Y. P. Chen, W. Duan, and S. Zhou, Robust gapless surface state and Rashba-splitting bands upon surface deposition of magnetic Cr on $Bi4_2Se_3$, Nano Lett. **15**, 2031 (2015).

[63] F. Pielmeier, G. Landolt, B. Slomski, S. Muff, J. Berwanger, A. Eich, A. A. Khajetoorians, J. Wiebe, Z. S. Aliev, M. B. Babanly, R. Wiesendanger, J. Osterwalder, E. V. Chulkov, F. J. Giessibl, and J. H. Dil, Response of the topological surface state to surface disorder in $TlBiSe_2$, New J. Phys. **17**, 023067 (2015).

[64] Y. Ren, T. Dai, W. Luo, and X. Liu, Evidences of sensitization mechanism for PbSe thin films photoconductor, Vacuum **149**, 190 (2018).

[65] K. Sakamoto, H. Matsuhata, K. Kyoya, K. M. Kazushi Miki, and T. S. Tsunenori Sakamoto, Abrupt Si/Ge/Si(001) interfaces fabricated with Bi as a surfactant, Jpn. J. Appl. Phys. **33**, 2307 (1994).

[66] S. W. Jun, C. M. Fetzer, R. T. Lee, J. K. Shurtleff, and G. B. Stringfellow, Bi surfactant effects on ordering in GaInP grown by organometallic vapor-phase epitaxy, Appl. Phys. Lett. **76**, 2716 (2000).

[67] R. D. Gann, J. Wen, Z. Xu, G. D. Gu, and J. A. Yarmoff, Surface restructuring in sputter-damaged $Bi_2Sr_2CaCu_2O_{8+\delta}$, Phys. Rev. B **84**, 165411 (2011).

[68] V. S. Stolyarov, S. Pons, S. Vlaic, S. V. Remizov, D. S. Shapiro, C. Brun, S. I. Bozhko, T. Cren, T. V. Menshchikova, E. V. Chulkov, W. V. Pogosov, Y. E. Lozovik, and D. Roditchev, Superconducting long-range proximity effect through the atomically flat interface of a Bi_2Te_3 topological insulator, J. Phys. Chem. Lett. **12**, 9068 (2021).

[69] M. Kisiel, K. Skrobas, and M. Jałochowski, Angle-resolved photoemission of ultrathin Pb films on Si(111)-(6 × 6) Au: Quantum size effect, Opt. Appl. **35**, 443 (2005).

[70] G. Schubert, H. Fehske, L. Fritz, and M. Vojta, Fate of topological-insulator surface states under strong disorder, Phys. Rev. B **85**, 201105(R) (2012).

[71] R. Queiroz, G. Landolt, S. Muff, B. Slomski, T. Schmitt, V. N. Strocov, J. Mi, B. B. Iversen, P. Hofmann, J. Osterwalder, A. P. Schnyder, and J. H. Dil, Sputtering-induced reemergence of the topological surface state in Bi_2Se_3, Phys. Rev. B **93**, 165409 (2016).

[72] F. R. McFeely, S. Kowalczyk, L. Ley, R. A. Pollak, and D. A. Shirley, High-resolution x-ray-photoemission spectra of PbS, PbSe, and PbTe valence bands, Phys. Rev. B **7**, 5228 (1973).

[73] J. Habinshuti, P. Capiod, T. H. Nguyen, Y. Justo, F. J. Avila, M. C. Asensio, F. Bournel, J.-J. Gallet, I. Vobornik, J. Fujii, A. Addad, K. Lambert, J. P. Nys, Y. Lambert, Z. Hens, A. Osherov, Y. Golan, O. Robbe, S. Turrell, and B. Grandidier, Phase transformation of PbSe/CdSe nanocrystals from core-shell to Janus structure studied by photoemission spectroscopy, Phys. Rev. B **87**, 184102 (2013).

[74] https://cc.dvo.ru.

[75] https://www.nusc.ru.